Evaluating using GoPro cameras and Tsai's calibration for video-based submerged river-bed reconstruction

Wei Li
Department of Civil & Environmental Engineering
University of Auckland
Auckland, New Zealand

Trevor Gee
Department of Computer Science
University of Auckland
Auckland, New Zealand

Patrice Delmas
Department of Computer Science
University of Auckland
Auckland, New Zealand

Heide Friedrich
Department of Civil & Environmental Engineering
University of Auckland

***Abstract*—In the last decade, consumer-grade waterproof digital cameras have been available more readily, allowing a more straight-forward application of underwater stereo photogrammetry, with the goal of obtaining high-quality DEMs. This paper presents our work into 3D river-bed reconstruction, using a GoPro Hero 3 black edition camera based on Tsai's calibration. The objective of this paper is to identify the performance of Tsai's calibration for underwater applications and provide other researchers with practical operation guidelines in respect to camera to object distance and various flow strengths encountered. We present the DEM results for a ground truth hemisphere model, chosen for its resemblance with packed natural water-worked gravel particles.**

Keywords—Tsai calibration; stereo photogrammetry; GoPro; hydraulic engineering

I. INTRODUCTION

Stereo photogrammetry techniques have been used more extensively for hydraulic engineering research in recent times. Massot-Campos and Oliver-Codina [1] are providing a summary of applications and solutions for underwater imaging. The popularity of stereo photogrammetry nowadays is due to: (i) ease of usability of consumer-grade cameras and (ii) free processing tools. Consumer-grade cameras, like the GoPro series' cameras, are affordable and conveniently available. Previous studies have used consumer cameras for the successful application of underwater calibration or scene reconstruction [2-5]. When it comes to processing stereo images, Bouguet's calibration toolbox, based on Zhang's calibration algorithm [6], is widely used and has been confirmed to be robust and accurate for various applications. In addition, other MATLAB toolboxes, such as the Computer Vision and Point Cloud toolboxes [7], allow a more user-friendly stereo image processing operation, overcoming the manual shortcomings.

For selected applications, with time, energy or space constraints, Tsai's calibration method however is more suited than Zhang's calibration method. In general, there are fewer implementations of Tsai's calibration. Li, et al. [8] provide a practical comparison of Tsai's and Zhang's calibration method, whilst Gee, et al. [9] provide a more detailed performance evaluation of Tsai's calibration method. The potential of Tsai's calibration method lies in a more efficient single-image calibration workflow, compared to the multiple-image based Zhang calibration workflow [6]. Thus Tsai's calibration is well-suited for applications that require real-time calibration, such as can be found in underwater hydraulic engineering research. In hydraulic engineering applications, changes in flow velocity, pressure, temperature and salinity alter the refraction index of water and thus the camera calibration parameters related to distortion, ideally requiring calibration results to be constantly modified [11]. There is a need for an efficient in-situ calibration method.

In the following we present a brief background of camera calibration basics in Section 2. Our workflow based on Tsai's calibration method is presented in Section 3. Section 4 provides information about the experimental laboratory setup and study methodology. Section 5 presents the results and discusses the performance of our stereo-vision workflow. Finally, Section 6 offers the concluding remarks.

II. BACKGROUND

A. Camera calibration under pinhole and radial distortion model

Camera calibration may be described efficiently using the pinhole camera model and a Tsai calibration distortion free model. Using homogeneous coordinates, consider a point P in the physical world, with coordinates $(X, Y, Z, 1)$ being projected onto the image plane at pixel location p given by $(x, y, 1)$:

$$p = K[R\ T]P, where, K = \begin{bmatrix} f_x & 0 & C_x \\ 0 & f_y & C_y \\ 0 & 0 & 1 \end{bmatrix} \quad (1)$$

978-1-5090-2748-4/16/$31.00 ©2016 IEEE

C_x and C_y are displacements coordinate's centre on the projection image plane, and f_x and f_y represent individual pixels, as for a typical low-cost camera sensor.

The rotation matrix R is $\begin{bmatrix} r_1 & r_2 & r_3 \\ r_4 & r_5 & r_6 \\ r_7 & r_8 & r_9 \end{bmatrix}$ and the translation vector T is $\begin{bmatrix} T_x \\ T_y \\ T_z \end{bmatrix}$. Furthermore, considering radial distortion in Tsai's calibration model, one can assume (x_d, y_d) to be the sensor coordinate related to the world coordinate (X, Y, Z), (δ_x, δ_y) to be the pixel size in X and Y direction, s_x to be a scale coefficient, κ_1, κ_2 to be the distortion coefficient.

The above parameters are connected by:

$$\delta_x x_d(1 + \kappa_1 r^2 + \kappa_2 r^4) = s_x f \frac{r_1 X_w + r_2 Y_w + r_3 Z_w + Tx}{r_7 X_w + r_8 Y_w + r_9 Z_w + Tz} \quad (2)$$

$$\delta_y y_d(1 + \kappa_1 r^2 + \kappa_2 r^4) = f \frac{r_4 X_w + r_5 Y_w + r_6 Z_w + Tx}{r_7 X_w + r_8 Y_w + r_9 Z_w + Tz} \quad (3)$$

When considering distortion, the distortion model is usually given as a mapping from the distorted image coordinates (x_d, y_d), which are observed in the images, to the undistorted image coordinates (x_u, y_u) that are not physically measurable. The mapping can be done with different models, suiting various lens types, causing different distortion.

We use a radial, decentering and prism distortion model as proposed by Brown [12], which has been extensively used previously to characterise distortion of images. More information in regards to the modifications undertaken can be read in [13]. For radial distortion, in practice, this distortion is small and can be characterised by the first terms of a Taylor series expansion. In general, the typical distortion model can be expressed by the following formula. Assume that the principal point is $(0,0)$.

$$\begin{bmatrix} x_u \\ y_u \end{bmatrix} = \begin{bmatrix} x_d \\ y_d \end{bmatrix} [1 + \kappa_1 r^2 + \kappa_2 r^4 + \kappa_3 r^6 + \cdots],$$

$$where\ r = \sqrt{{X_d}^2 + {Y_d}^2} \quad (4)$$

Here, (x_d, y_d) is the original location of the distorted point and (x_u, y_u) is the corrected point.

III. METHODOLOGY

A. Underwater calibration

Underwater refraction, caused by imaging through an air-solid-water interface, produces non-linear deformations in the images captured. Such refraction results in mathematical non-collinearity [14]. Menna, et al. [15] review how the camera housing, generally designed as a flat port or a dome port, further affects the distortion model, FOV and focus length.

The refraction effect leading to changing focus length and Field of View (FoV) is illustrated in Fig. 1. As can be seen, the FoV has been largely reduced from 122.6 degrees in-air to 92 degrees underwater for the GoPro Hero 3 black edition camera. A flat port housing is used in the present study.

According to the study by Menna, et al. [15], the primary effect of refraction through the air-solid and solid-water interfaces is radially symmetric around the principal point, which is absorbed by the radial lens distortion component. Menna, et al. [16] evaluate whether decentering distortion parameters can absorb systematic errors that could not be modelled by the collinearity equation model. Chan, et al. [4] state that the focal length for underwater calibration increases by a factor of 1.333, which is the refraction index of water. Moreover, the image centre of the camera lens is found to be identical for the in-air and underwater situation. However, although Rahman, et al. [17] shows that focus length and image centre adjustments take place, the reprojection error for underwater calibration is better than in-air.

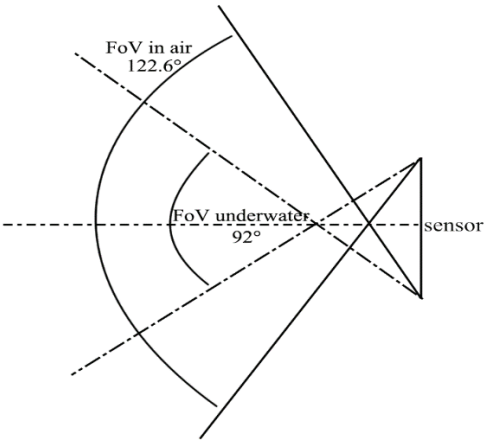

Fig. 1. Underwater pinhole model, with the different Field of Views (FoVs) for GoPro 3 Hero 3 black edition in-air and underwater.

Furthermore, for underwater studies, refraction will be also affected by non-uniformities in the flow, the attenuation of light and potential image blurring. Herewith we will in particular study how flow velocity affects the calibration results. The attenuation of light is related to the depth of water. Our environment is a shallow water environment, we consider the camera depth to the water surface and the distance from the camera to the viewing target. Blurred images of underwater scenes can have several causes, and potentially affect the accuracy of the corner detection. Conventionally, an OpenCV function for extracting chequerboard corners is widely used, yet the algorithm can fail under complex illumination and deformation conditions. Other corner detection methods are available for underwater studies [8].

B. Stereo rectification and matching

Stereo rectification is based on epipolar geometry, which describes the basic geometry of a stereo image system. Cameras will almost never be exactly aligned in the frontal parallel configuration, thus finding mathematically image projections and distortion maps to rectify the left and right images is important for preparing a frontal parallel arrangement. Fusiello's [19] rectification algorithm is designed to tackle this task.

During stereo matching, the corresponding pixels from the rectified left and right images are identified, by warping the images to align the pixels on the same line. It is important to compute the disparity based on accurate stereo matching results. There is a large number of stereo matching algorithms available for various application. For our hydraulic engineering

applications, we are in particularly interested in studying gravel beds, and special conditions for stereo matching have to be considered for this kind of environment. For example, the monotone texture and the irregular shape of the gravel particles would affect the performance of the stereo matching. Being both robust to illumination variation within a stereo pair as well as some level of non-epipolar alignment, the symmetric dynamic programming stereo (SDPS) matching algorithm [20] is suited for our hydraulic application, and was confirmed to obtain accurate results [21, 22].

C. Underwater image processing

Underwater imaging is challenging [1]. Insufficient illumination and wavelength-dependent light absorption can result in not well-lit images [23]. Moreover, the complexity of the air-solid-water interface affects the camera's intrinsic parameters, and thus provides more challenges for the cameras' calibration [24] and image processing algorithms [25, 26]. Additionally, images taken in shallow waters can be affected strongly by flickering, light fluctuation due to the sunlight's refraction on a wavy water surface, as discussed in [27].

In our study we applied the Retinex algorithm to improve both the calibration images and the target images. The Retinex algorithm, original proposed by Edward Land in 1986, is a model of human perception of light and colour, and is one method to enhance the digital image quality. Currently, implementations of Retinex are summarised in Analysa's study [28]. The advantage to add Retinex to a stereo-vision workflow is the adjustments of the parameters controlling the Gaussian filter and dynamic features, resulting in a better fit for SDPS algorithm. Moreover, an improvement to Bertin's method [22] to using Retinex considering both the area of interest (AOI) and exposure evaluation area is confirmed to be beneficial improving the stereo matching accuracy.

D. Accuracy evaluations

Reprojection error and rectification error are used to evaluate the accuracy of calibration and the accuracy of stereo workflow. The accuracy of the calibration is usually evaluated by the reprojection error, E_d, which is measured as the discrepancy between observed pixel coordinate, (x_{pi}, y_{pi}), and the estimated pixel coordinate, $(\hat{x}_{pi}, \hat{y}_{pi})$, by projecting the measured world coordinate by the model of camera with distortion.

$$E_d = \frac{1}{n}\sum_{i=1}^{n}\sqrt{(\hat{x}_{pi} - x_{pi})^2 + (\hat{y}_{pi} - y_{pi})^2} \quad (5)$$

The rectification error, E_r, which is measured as the discrepancy in y coordinates between the corresponding left pixel coordinate, (x_{li}, y_{li}), and the right pixel coordinate, (x_{ri}, y_{ri}), after adjusting the camera matrix to achieve frontal parallel. The rectified pair of images can only deliver accurate stereo matching, when the rectification error is minimal, usually below 1 pixel. The rectification error is evaluated with

$$E_r = \frac{1}{n}\sum_{i=1}^{n}|y_{li} - y_{ri}| \quad (6)$$

IV. Experimental Methodology

A. Experimental environment

We conducted our studies in a 19.6 m long, 0.545 m wide and 0.58 m deep hydraulic flume available in the Hydraulic Engineering Laboratory at the University of Auckland. Two xenon lights are set up at the test section of each side along the flume. In order to get a uniform illuminated environment, two reflectors are used to avoid directly illuminating the region of interest in the flume, as shown in Fig. 2. We also have found that xenon lights prevent the flickering effect for video recording.

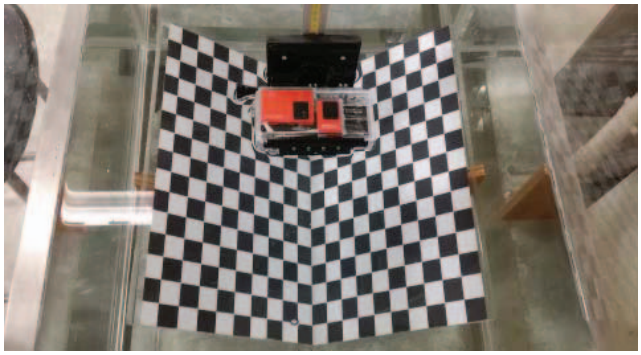

Fig. 2. Experimental environment, plane view of region of interest in the hydraulic flume.

We used GoPro Hero 3 black edition cameras for video acquisition. There are two reasons to use video instead of photo in our study for the calibration and measurement stages separately. For the calibration stage, using multiple frames reduces the likelihood of unsatisfactory chequerboard image quality, which could potentially lead calibration failure. For the measurement stage, continuous information is required to study our dynamic processes. The Gopro Hero 3 black edition camera provides several video formats with various choices of resolution, field of view and framerate. Past studies used the GoPro 3 video recording format with a resolution of 1920*1080 pixel [29]. For our study we chose a resolution of 1920*1440 pixel, making full use of the view of range of the sensor, as shown in Fig. 2. At this resolution, a maximum 48fps can be sampled.

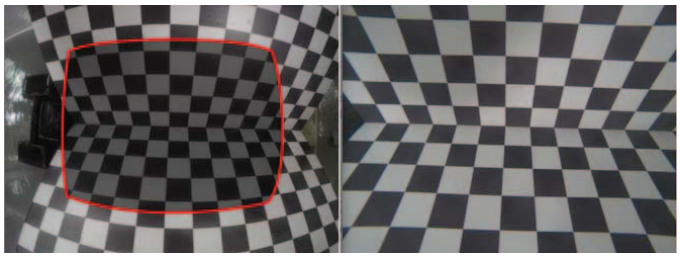

Fig. 3. Distortion for GoPro Hero 3 black edition camera in-air (left), and underwater (right). The red frame overlaid in-air shows the equivalent FoV underwater.

An accurate non-planar chequerboard is used for Tsai's calibration workflow. Our non-planar chequerboard is 450 mm wide. The chequerboard is printed on water-proof paper and laminated, with 19 horizontal squares and 14 vertical squares, with square sizes of 30 mm. We have found that the laminating material should not be glossy to prevent reflection. With the chequerboard placed at the bottom of the hydraulic flume, the depth range covered is around 210 mm. The pose of the chequerboard is placed in flow direction, thus reducing the flow's disturbance in the hydraulic flume. A heavy thin metal base is used to stabilise the chequerboard during high flows.

B. Experimental process

We studied Tsai's calibration accuracy for 9 different camera to object distances, namely H1(250), H2(240), H3(230), H4(220), H5(210), H6(200), H7(190), H8(180) and H9(170), with distances in brackets in mm. Besides studying the suitability of Tsai's calibration for underwater environment, an important consideration for hydraulic engineering research is the effect the flow velocity has on stereo-vision data quality. Thus a calibration evaluation experiment based on seven different flow velocities, and a still flow (S), as shown in Table □, was designed.

TABLE I. FLOW VELOCITIES

	S	F1	F2	F3	F4	F5	F6	F7
Velocity m/s	0	0.07	0.15	0.20	0.33	0.41	0.51	0.58

The operation of the GoPro cameras was controlled by WiFi, and thus the cameras were set up 100 mm below water surface to allow for WiFi communication. The WiFi wavelength signal is 2.4Ghz, hence a wavelength of 125 mm suggests that the cameras should be placed less than 125 mm below water surface.

V. RESULTS AND DISCUSSION

A. Underwater image quality

Fig. 4 shows an example of the images acquired during the calibration testing. There are two aspects to be noted:

- Blurring: Underwater images are usually blurred due to attenuation of light. Chan, et al. [4] did state that the water-proof housing could be the reason for the blur found in GoPro images.
- Chromatic dispersion: Chromatic dispersion is visible at the border of the taken images, leading to a large shift in lines and corners at the image's edges. Normal corner detection algorithms detect corners in grey level images, after converting from the original colour image. With chromatic dispersion inconsistent corner detection can occur accounting for red, green and blue channels.

To improve the corner selection process, an image sharpness filter is used to process the chequerboard images. Retinex is also applied for underwater images [30]. However, such image processing method still can not deal with chromatic dispersion, which is due to light rays', when refracted, separation into different wavelengths of the visible colour spectrum, causing a loss of sharpness and colour saturation. We carefully choose corners to decrease the influence, and further use a sharpness filter to increase the corner detection accuracy. Fig. 4 also shows the corners selected for the corresponding left and right chequerboard image, not considering the border corners, due to uncertainty in accurate detection.

Out of a possible 234 corners, the number of corners used for the corner detection algorithm at the various distances are H1(83), H2(53), H3(53), H4(53), H5(46), H6(46), H7(39), H8(39) and H9(28). The difference in the corner numbers is due to the changing FoV. We were selective in only choosing corners for calibration that were not affected by blurring and chromatic dispersion.

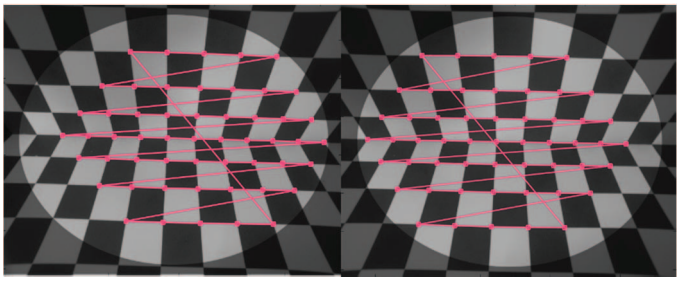

Fig. 4. Corner selection for the stereo pair ignoring blurred and chromatic dispersed corners. Corners selected on the left image (left). Corners selected one the corresponding right image (right).

B. Underwater calibration results

The reprojection errors for the left and right camera at different flow velocity and different distance to calibration chequerboard are shown in Table □ and Table □. We observed that the underwater environment has an effect on the image quality, and thus being selective on the corners chosen for calibration proved important to ensure Tsai's calibration success.

The underwater refraction distortion was absorbed into the distortion model of Tsai's calibration method in our study. Gupta, et al. [14] mentions that Tsai's method would also face the problem of mathematical non-collinearity from the non-linear deformations of the images. However, our experimental results, Tables □ and □, show a comparably constant reprojection error for the left and right cameras at different flow velocities. Our calibration results show that flow velocity does not affect reprojection errors substantially, with the error being around 0.1 mm. Since we assured that camera and calibration target were fixed at all times, only a change in corner detection caused by varying image quality and illumination under changing flow velocity contributes to the slight observed change in error. However, the camera to object distance has a bigger effect on reprojection error, mainly due to the varying number of corners available for calibration. However, even a comparably small number of corners can still achieve good calibration results. A similar study, based on Zhang's calibration, shows that the calibration parameters, including the focus length and distortion coefficients, differed for still water and 0.05 m/s flow [31]. Yet no information was available about the underwater calibration process, similar to the study by Chan, et al. [4]. Table □ shows the rectification error. Here the effect of the camera to object distance is visible.

C. Underwater reconstruction results

To validate the calibration results for DEM reconstruction, we placed a hemisphere model, also a known ground truth that resembles the arrangement of smooth river pebbles, underwater. Fig. 5 shows the reconstructed DEM with DEM of difference (DoD). A mean error of 1.10 mm ± 1.06 mm is obtained for the underwater measurements, compared to 1.81 mm ± 1.57 mm for in-air. Improved accuracy can be achieved for underwater DEM reconstruction when one considers a narrower FoV with corresponding higher resolution for the region of interest (ROI). Essentially reducing the distortion, and improving the successful

application of Tsai's radial distortion model. To put our results in perspective, Schmidt and Rzhanov [5] used GoPro cameras to perform micro bathymetry and achieve a resolution of 3 mm for their reconstructions. The final DEM reconstruction shows that Tsai's calibration is suited when combined with GoPro Hero 3 black edition cameras for video acquisition in the quest to reconstruct 3D underwater river beds.

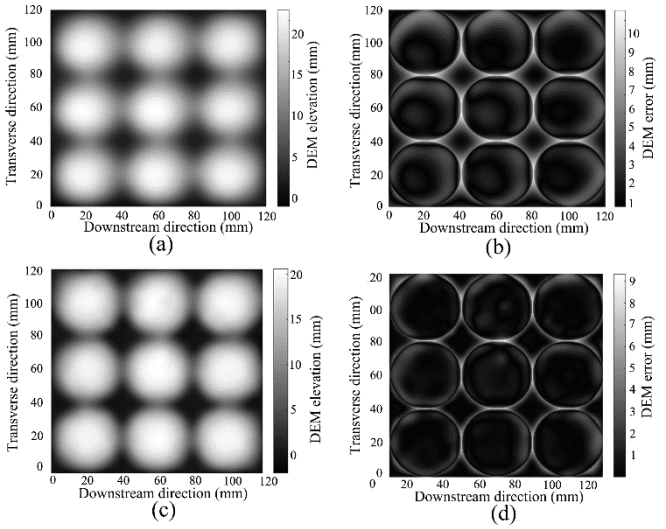

Fig. 5. DEM of the hemisphere model in-air (a) and underwater (c), with corresponding DoD in-air (b) and underwater (d).

VI. Conclusion

An overview and evaluation of combining GoPro Hero 3 black edition cameras and Tsai's calibration has been presented for submerged conditions. Details of the water-proof chequerboard design, video mode choice, effective WiFi distance and effective corner selection will provide useful guidelines for other researchers wishing to proceed with similar underwater applications. Besides testing the suitability of Tsai's calibration, we in particularly evaluated the effect of flow velocity and distance between camera and object.

Our results show that for our study environment, a laboratory hydraulic flume, obtained calibration parameters are relatively constant in flows up to 0.6 m/s. Increasing the distance between camera and object contributes to a minor increase in reprojection and rectification errors. Furthermore, our work highlights the importance of the chequerboard to be suitably designed for changing flow and camera to object distances, as the number of corners used as well as the position of corners is a major factor affecting the final DEM reconstruction using Tsai's calibration. Under moving water condition, it is furthermore important to secure the calibration object, and have a stable camera setup, restricting movement. For our tested camera system, GoPro Hero 3 black edition, going underwater is improving on the in-air capabilities for close-range stereo-vision, absorbing the refraction distortion by GoPro's 3D box. We will continue working on improving the present workflow to better facilitate a complete calibration process for hydraulic engineering applications.

Acknowledgment

The study was partly funded by the Marsden Fund (Grant No. UOA1412), administered by the Royal Society of New Zealand. Wei Li is supported by the New Zealand China Doctoral Research Scholarship (NZCDRS) from the Ministry of Foreign Affairs and Trade.

References

[1] M. Massot-Campos and G. Oliver-Codina, "Optical Sensors and Methods for Underwater 3D Reconstruction," *Sensors,* vol. 15, pp. 31525-31557, 2015.

[2] J.-M. Lavest, G. Rives, and J.-T. Lapresté, "Dry camera calibration for underwater applications," *Machine Vision and Applications,* vol. 13, pp. 245-253, 2003.

[3] N. B. Hui and D. K. Pratihar, "Camera calibration using a genetic algorithm," *Engineering Optimization,* vol. 40, pp. 1151-1169, 2008.

[4] Y. H. Chan, M. Nguyen, A. Gastelum, S. Yang, R. Gong, N. Liu*, et al.*, "The Ngongotaha river UDPS experiment: low-cost underwater dynamic stereo photogrammetry," in *Proceedings of the 27th Conference on Image and Vision Computing New Zealand*, 2012, pp. 412-417.

[5] V. E. Schmidt and Y. Rzhanov, "Measurement of micro-bathymetry with a GOPRO underwater stereo camera pair," in *Oceans, 2012*, 2012, pp. 1-6.

[6] Z. Zhang, "A flexible new technique for camera calibration," *Pattern Analysis and Machine Intelligence, IEEE Transactions on,* vol. 22, pp. 1330-1334, 2000.

[7] G. Bradski, "The opencv library," *Doctor Dobbs Journal,* vol. 25, pp. 120-126, 2000.

[8] W. Li, T. Gee, H. Friedrich, and P. Delmas, "A practical comparison between Zhang's and Tsai's calibration approaches," in *Proceedings of the 29th International Conference on Image and Vision Computing New Zealand*, 2014, p. 166.

[9] T. Gee, P. Delmas, N. Stones-Havas, C. Sinclair, W. Van Der Mark, W. Li*, et al.*, "Tsai camera calibration enhanced," in *Machine Vision Applications (MVA), 2015 14th IAPR International Conference on*, 2015, pp. 435-438.

[10] J. Heikkila, "Geometric camera calibration using circular control points," *Pattern Analysis and Machine Intelligence, IEEE Transactions on,* vol. 22, pp. 1066-1077, 2000.

[11] P. Schiebener, J. Straub, J. L. Sengers, and J. Gallagher, "Refractive index of water and steam as function of wavelength, temperature and density," *Journal of physical and chemical reference data,* vol. 19, pp. 677-717, 1990.

[12] D. C. Brown, "Decentering distortion of lenses," *Photometric Engineering,* vol. 32, pp. 444-462, 1966.

[13] J. Weng, P. Cohen, and M. Herniou, "Camera calibration with distortion models and accuracy evaluation," *IEEE Transactions on pattern analysis and machine intelligence,* vol. 14, pp. 965-980, 1992.

[14] M. Gupta, S. Upadhyay, S. Sigh, and A. Ngawat, "Camera Calibration Technique Using Tsai's Algorithm," *IntJthisnal of Enterprise Computing and Business Systems,* 2011.

[15] F. Menna, E. Nocerino, F. Fassi, and F. Remondino, "Geometric and optic characterization of a hemispherical dome port for underwater photogrammetry," *Sensors,* vol. 16, p. 48, 2016.

[16] F. Menna, E. Nocerino, S. Troisi, and F. Remondino, "A photogrammetric approach to survey floating and semi-submerged objects," in *SPIE Optical Metrology 2013*, 2013, pp. 87910H-87910H-15.

[17] T. Rahman, J. Anderson, P. Winger, and N. Krouglicof, "Calibration of an underwater stereoscopic vision system," in *2013 OCEANS-San Diego*, 2013, pp. 1-6.

[18] B. K. Horn, "Tsai's camera calibration method revisited," *Online: http://people. csail. mit. edu/bkph/articles/Tsai_Revisited. pdf,* 2000.

[19] A. Fusiello, E. Trucco, and A. Verri, "A compact algorithm for rectification of stereo pairs," *Machine Vision and Applications,* vol. 12, pp. 16-22, 2000.

[20] G. Gimel'farb, "Probabilistic regularisation and symmetry in binocular dynamic programming stereo," *Pattern Recognition Letters,* vol. 23, pp. 431-442, 2002.
[21] S. Bertin and H. Friedrich, "Measurement of gravel-bed topography: evaluation study applying statistical roughness analysis," *Journal of Hydraulic Engineering,* vol. 140, pp. 269-279, 2014.
[22] S. Bertin, H. Friedrich, P. Delmas, E. Chan, and G. Gimel'farb, "Digital stereo photogrammetry for grain-scale monitoring of fluvial surfaces: Error evaluation and workflow optimisation," *ISPRS Journal of Photogrammetry and Remote Sensing,* vol. 101, pp. 193-208, 2015.
[23] R. M. Pope and E. S. Fry, "Absorption spectrum (380–700 nm) of pure water. II. Integrating cavity measurements," *Applied optics,* vol. 36, pp. 8710-8723, 1997.
[24] C. Beall, B. J. Lawrence, V. Ila, and F. Dellaert, "3D reconstruction of underwater structures," in *Intelligent Robots and Systems (IROS), 2010 IEEE/RSJ International Conference on*, 2010, pp. 4418-4423.
[25] Y. Y. Schechner and N. Karpel, "Clear underwater vision," in *Computer Vision and Pattern Recognition, 2004. CVPR 2004. Proceedings of the 2004 IEEE Computer Society Conference on*, 2004, pp. I-536-I-543 Vol. 1.
[26] M. Roser, M. Dunbabin, and A. Geiger, "Simultaneous underwater visibility assessment, enhancement and improved stereo," in *2014 IEEE International Conference on Robotics and Automation (ICRA)*, 2014, pp. 3840-3847.
[27] N. Gracias, S. Negahdaripour, L. Neumann, R. Prados, and R. Garcia, "A motion compensated filtering approach to remove sunlight flicker in shallow water images," in *OCEANS 2008*, 2008, pp. 1-7.
[28] A. M. Gonzales and A. M. Grigoryan, "Fast Retinex for color image enhancement: methods and algorithms," in *IS&T/SPIE Electronic Imaging*, 2015, pp. 94110F-94110F-12.
[29] T. Dolereit, U. F. von Lukas, and A. Kuijper, "Underwater stereo calibration utilizing virtual object points," in *OCEANS 2015-Genova*, 2015, pp. 1-7.
[30] X. Fu, P. Zhuang, Y. Huang, Y. Liao, X.-P. Zhang, and X. Ding, "A retinex-based enhancing approach for single underwater image," in *2014 IEEE International Conference on Image Processing (ICIP)*, 2014, pp. 4572-4576.
[31] Y. J. Pang, D. Wang, H. Huang, and M. W. Sheng, "Research on Underwater Binocular Camera Calibration and Distortion Analysis in Current Disturbance," in *Applied Mechanics and Materials*, 2014, pp. 688-692.

TABLE II. REPROJECTION ERROR FOR THE LEFT CAMERA

	Left Reprojection Error (mm)																	
	H1		H2		H3		H4		H5		H6		H7		H8		H9	
	Avg	Std	Avg	Std	Avg	Std	Avg	Std	Avg	Std	Avg	Std	Avg	Std	Avg	Std	Avg	Std
S	0.88	0.33	1.20	0.27	1.10	0.30	1.10	0.35	1.20	0.18	1.10	0.20	1.20	0.24	1.20	0.28	1.60	0.42
F1	0.89	0.33	1.21	0.27	1.09	0.29	1.11	0.36	1.21	0.17	1.10	0.19	1.20	0.23	1.20	0.26	1.61	0.42
F2	0.89	0.33	1.20	0.26	1.10	0.31	1.10	0.35	1.20	0.18	1.09	0.20	1.21	0.24	1.21	0.29	1.60	0.41
F3	0.86	0.31	1.21	0.24	1.10	0.30	1.09	0.36	1.19	0.16	1.11	0.21	1.17	0.22	1.22	0.28	1.60	0.40
F4	0.89	0.33	1.21	0.27	1.09	0.29	1.10	0.35	1.17	0.15	1.12	0.21	1.20	0.24	1.20	0.26	1.62	0.42
F5	0.89	0.33	1.20	0.26	1.10	0.31	1.11	0.36	1.20	0.17	1.10	0.19	1.21	0.25	1.22	0.28	1.61	0.41
F6	0.88	0.33	1.21	0.24	1.10	0.30	1.10	0.35	1.20	0.18	1.10	0.20	1.19	0.24	1.20	0.28	1.63	0.43
F7	0.86	0.33	1.20	0.23	1.11	0.31	1.10	0.36	1.20	0.17	1.11	0.21	1.20	0.23	1.21	0.27	1.63	0.42

TABLE III. REPROJECTION ERROR FOR THE RIGHT CAMERA

	Right Reprojection Error (mm)																	
	H1		H2		H3		H4		H5		H6		H7		H8		H9	
	Avg	Std	Avg	Std	Avg	Std	Avg	Std	Avg	Std	Avg	Std	Avg	Std	Avg	Std	Avg	Std
S	0.95	0.51	1.20	0.28	1.30	0.30	1.20	0.36	1.20	0.39	0.99	0.27	1.20	0.26	1.20	0.28	1.00	0.21
F1	1.0	0.45	1.21	0.29	1.29	0.29	1.20	0.37	1.19	0.38	0.99	0.28	1.21	0.26	1.21	0.27	1.01	0.22
F2	1.1	0.45	1.20	0.26	1.31	0.30	1.20	0.36	1.20	0.39	1.00	0.27	1.20	0.25	1.20	0.28	1.01	0.21
F3	1.0	0.44	1.22	0.28	1.30	0.30	1.20	0.38	1.22	0.42	1.01	0.28	1.21	0.26	1.21	0.29	1.02	0.23
F4	1.1	0.45	1.20	0.29	1.31	0.32	1.20	0.36	1.20	0.40	1.02	0.29	1.20	0.24	1.20	0.28	1.01	0.21
F5	1.1	0.45	1.21	0.28	1.30	0.31	1.20	0.35	1.21	0.39	1.00	0.27	1.20	0.26	1.22	0.30	1.01	0.22
F6	1.1	0.45	1.19	0.27	1.32	0.30	1.20	0.36	1.20	0.40	1.02	0.27	1.21	0.26	1.23	0.31	1.02	0.23
F7	1.0	0.45	1.20	0.26	1.31	0.31	1.20	0.39	1.23	0.41	1.02	0.28	1.22	0.27	1.22	0.29	1.03	0.23

TABLE IV. RECTIFICATION ERROR FOR THE SETUP

	Rectification Error (pixel)																	
	H1		H2		H3		H4		H5		H6		H7		H8		H9	
	Avg	Std	Avg	Std	Avg	Std	Avg	Std	Avg	Std	Avg	Std	Avg	Std	Avg	Std	Avg	Std
S	1.22	0.99	0.64	0.55	0.73	0.64	1.06	0.70	1.15	1.08	0.86	0.70	0.94	0.70	1.20	0.91	0.91	0.85
F1	1.26	1.05	0.66	0.57	0.74	0.65	1.08	0.72	1.16	1.08	0.88	0.72	0.95	0.72	1.21	0.92	0.93	0.85
F2	1.27	1.09	0.65	0.58	0.74	0.63	1.08	0.74	1.17	1.09	0.89	0.74	0.97	0.74	1.23	0.92	0.95	0.86
F3	1.29	1.09	0.67	0.58	0.76	0.65	1.09	0.74	1.19	1.10	0.91	0.76	0.97	0.74	1.23	0.93	0.97	0.87
F4	1.29	1.08	0.68	0.57	0.77	0.64	1.10	0.76	1.19	1.10	0.91	0.76	0.98	0.75	1.25	0.95	0.97	0.86
F5	1.29	1.09	0.69	0.59	0.77	0.65	1.10	0.75	1.21	1.11	0.92	0.77	0.99	0.77	1.28	0.97	0.98	0.86
F6	1.31	1.11	0.69	0.59	0.78	0.67	1.11	0.77	1.22	1.12	0.93	0.78	1.02	0.78	1.29	0.98	1.02	0.89
F7	1.30	1.11	0.69	0.60	0.80	0.69	1.13	0.77	1.22	1.12	0.92	0.78	1.02	0.78	1.28	0.98	1.05	0.92